A Novel Multidimensional Perspective on Dynamic Characteristics of the Peculiar Feather-Shaped Dunes in Kumtag Desert With Time-Series Optical and SAR Observations

Chao Ding, Guangcai Feng, Lu Zhang, and Mingsheng Liao

***Abstract*—As a world-class problem that has confused the field of geoscience for a long time, the formation mechanism of the peculiar feather-shaped dunes in Kumtag Desert has not been clarified due to the deficiency of a comprehensive investigation on the dune dynamic characteristics. Because of the quickly changeable dune morphology and sands' low dielectric constants, the traditional single technique generally was only used to identify or quantify dune mobility in one or two dimensions, and cannot retrieve the complete information of dune dynamic characteristics. To overcome these deficiencies, a comprehensive study of confusing the optical image cross-correlation, synthetic aperture radar (SAR) offset-tracking, and small baseline subsets interferometric SAR (InSAR) and InSAR coherence was performed here to identify and quantify the movements of feather-shaped dunes from a mutidimensional (East–West, North–South, slant-range, azimuth, and coherence) perspective. These results showed that the feather-shaped dunes demonstrate a movement tendency from the northeastern to the southwestern orientation (204.32° ± 52.15°) with the displacement magnitude of 3.34 ± 2.26 m/year, in consistent with the predominant wind condition. Specifically, the spatial heterogeneity was found that these dunes move along a relatively small slope gradient (0°–6°) and a northwestern–southeastern facing slope aspect (300°–350°, 120°–180°). Besides, the large displacement velocities are mainly concentrated in the pinna rachis rather than the rami of the feather-shaped dunes. This article sheds a light on the comprehensive investigation on the large-scale dynamic characteristics of peculiar feather-shaped dunes by combining the medium-resolution optical and SAR satellite observations.**

***Index Terms*—Feather-shaped dunes, Kumtag Desert, multidimensional dynamic characteristics, optical image cross-correlation, synthetic aperture radar (SAR), spatiotemporal evolution.**

I. Introduction

LIMITED by the long-term constraints of the Qinghai–Tibet Plateau and the Siberian Mongolian high pressure, the climate of northwestern China was characterized by drought and windy all over the year. Such harsh climatic conditions contribute to a wide range of mobile deserts in this region, such as the Taklamakan Desert which is famous as the largest mobile desert in China, as well as the Tengger Desert, Kumtag Desert, Badain Jaran Desert, and Ulan Bu Desert. As a product of aeolian processes in active deserts, sand dunes in windy environments generally maintained the moving state through the wind erosion on the windward slope and the sedimentation processes on the leeward slope [1], [2]. The mobile dunes may invade the oasis farmland, water sources, human settlements, and surrounding infrastructures in the downstream area [3], and release a large amount of suspended sand particles to trigger disastrous weather and serious air pollution, such as the sand–dust storm [4], [5], [6].

From the perspective of meteorological dynamics, the movement rates of sand dunes show a linear proportional relationship with the cube of wind shear rate [5], [7], [8], and thus keenly reflect the physical attributes and changes of wind-blown sand flow over the dunes' surface [9], [10]. Thus, the velocity of dune movement is an important geomorphological indicator for revealing out the potential atmospheric disasters, such as the sand/dust storms. Moreover, the velocity of dune movement can be utilized to derive the sand flux for better understanding the temporal change characteristics of sand transport [11]. Currently, these methods for measuring the dune movements can be generally divided into the field measurement and visual analysis on multitemporal remote sensing images. Even though possessing the capability of accurately measuring the dune feature points, the traditional field techniques (levels, rules, theodolite, total stations, etc.) have the disadvantages of sparse spatial sampling density and high operating cost, far from meeting the requirements of monitoring the dune fields or deserts with a large geographical coverage [1], [12].

Manuscript received 7 January 2024; revised 28 February 2024 and 24 April 2024; accepted 10 June 2024. Date of publication 14 June 2024; date of current version 1 July 2024. This work was supported in part by the Open Research Fund Program of LIESMARS under Grant 22R03, in part by the National Natural Science Foundation of China under Grant 42304039, and in part by the Shandong Provincial Natural Science Foundation under Grant ZR2021QD075. *(Corresponding author: Chao Ding.)*

Chao Ding is with the School of Civil Engineering and Geomatics, Shandong University of Technology, Zibo 255049, China, and also with the State Key Laboratory of Information Engineering in Surveying, Mapping and Remote Sensing, Wuhan University, Wuhan 430079, China (e-mail: dingchao_sdut@163.com).

Guangcai Feng is with the School of Geosciences and Info-Physics, Central South University, Changsha 410083, China (e-mail: fredgps@csu.edu.cn).

Lu Zhang and Mingsheng Liao are with the State Key Laboratory of Information Engineering in Surveying, Mapping and Remote Sensing, Wuhan University, Wuhan 430079, China (e-mail: luzhang@whu.edu.cn; liao@whu.edu.cn).

This article has supplementary downloadable material available at https://doi.org/10.1109/JSTARS.2024.3414449, provided by the authors.

Digital Object Identifier 10.1109/JSTARS.2024.3414449

With the higher spatial–temporal monitoring density in a wide range of harsh environmental areas, the optical and radar remote sensing techniques have a great significance for reducing the workload of traditional field surveys. Among them, optical remote sensing is widely used to measure the dune movements with the visual interpretation and autonomous matching methods, because of its shorter revisit period and the specific imaging mode in accordance with the human eye [13]. Thus, the optical images have been widely used to monitor mobile deserts for a long time [14]. With the improvement of calculating capability, the multitemporal optical image cross-correlation technique has gradually liberated researchers from the heavy workload of manual interpretation. Initially, researchers measured the dune displacements based on the end-to-end optical images in the order of observation time sequence. For example, Vermeesch and Drake [15] studied the movement velocity of massive crescent dunes in the Bodri Depression of Chad with four ASTER images. Necsoiu et al. [16] analyzed the migration activity of near-polar dune fields based on the heterologous optical datasets of ASTER and SPOT-5. Hermas et al. [17] used two SPOT-4 panchromatic images to study the migration velocity and pattern of sand dunes in the Sinai Peninsula of Egypt. By combining the image cross-correlation, multiband analysis, and geographic information system (GIS) digitization, Scheidt and Lancaster [18] analyzed the interannual variations of dune migration in the southwestern of the Namib Desert. Bridges et al. [19] analyzed the differences of the dune dynamics between Mars and Earth with the HiRISE images.

However, with the continuous enrichment of optical datasets and the human attentions on the living environments, measuring dune displacements and evaluating the desertification process over a longer temporal scale have become the key emphasis of subsequent studies. For example, Vermeesch and Leprince [8] used seven optical images from different optical sensors to reveal out the evolution of dune migration in Central Sahara over nearly half a century. With the HiRISE imagery, Ayoub et al. [11] calculated the sand flux and analyzed the seasonal variation of Martian sand ripples. Based on the redundant observations of Landsat-8 and Sentinel-2 (S2) images, Ding et al. [20] and Ali et al. [21] successively proposed some innovative image pairing strategies to perform surface displacement time-series inversion for the mobile deserts in China and Egypt, respectively. Subsequently, Ding et al. [22] designed a method of fusing heterologous optical datasets to study the spatiotemporal patterns of dune mobility near Dunhuang City over a time span of around five years.

Compared to the widely used optical remote sensing technology, the synthetic aperture radar (SAR) possesses the advantages of less cloud disturbances, imaging in daytime and nighttime, and dense temporal sampling [23]. Thus, SAR has been used in the study of dune morphology, classification, and mobility [24]. For example, the utilization of the shuttle radar topography mission (SRTM) digital elevation model (DEM) dataset was employed by Blumberg [25] to assess the vertical dimensions and spatial distribution of the mega dunes. Subsequently, utilizing the valuable phase information, interferometric SAR (InSAR) was used to examine the alterations in both volume and height of sand dunes [26], [27], [28]. As an important component of InSAR measurement, the InSAR coherence also has been validated as an effective tool for detecting, mapping, and demonstrating the morphological changes of sand dunes [29], [30], [31]. Nevertheless, this coherence technology is suitable for identifying active dune fields and deriving a classification on the dune morphology, but not measuring the dune displacements. To achieve the quantification of dune mobility, Delgado Blasco et al. [32] designed an adaptive algorithm incorporating the GIS tools to measure the dune migration rates on the isolated barchan dunes by exploiting C-band Sentinel-1 (S1) satellite data. However, analogous to the manual delineation of dune outlines with optical images, this method is also characterized by a low degree of automation.

Under the common conditions, due to the low roughness and small dielectric constant of sand grains in dunes, these radar reflection signals usually present as the very weak and dim texture in SAR images. Comparatively, some specific dune structures, such as the linear and star-shaped dunes, display as the strong and easily identified reflection characteristics in SAR images [33], just like the dihedral and trihedral reflectors. However, there are few studies of measuring the dune displacements by performing the conventional InSAR or SAR offset-tracking with these radar strong scattering points. Different from other deserts, the unique "feather-shaped" dunes were widely distributed in Kumtag Desert, possessing the structural characteristics of both longitudinal and star-shaped dunes [34]. In this article, these pinna rachises of the feather-shaped dunes were found presented as the strong and stable reflective signals in original SAR amplitude image, distinguished from the dim signals of surrounding ground features. These strong scattering points may provide a great convenience for validating the effectiveness of InSAR and SAR offset-tracking techniques in quantifying the movements of the feather-shaped dunes.

In summary, the technical approaches of combining the optical and SAR observations still have enormous potentials in quantifying the spatiotemporal law of mobile dunes and thus investigate the formation mechanism of specific dune morphology. In this article, by combining the optical image cross-correlation, SAR offset-tracking, small baseline subsets (SBAS) InSAR, and InSAR coherence time series, a methodology was proposed to study the multidimensional dynamic characteristics and their spatiotemporal evolution of the peculiar feather-shaped dunes in Kumtag Desert.

The rest of this article is organized as follows. The study region and laboratory datasets were described in Section II. Subsequently, the processing flows of the methodology, including optical image cross-correlation, SAR offset-tracking, SBAS-InSAR, coherence evaluation, and three-dimensional (3D) displacement velocity inversion of the feather-shaped dunes were detailed in Section III. The optical and SAR-derived results were presented and validated in Section IV. The discussions on the feasibility of measuring the multidimensional dynamic patterns of the peculiar feather-shaped dunes in Kumtag Desert by combing optical and SAR observations were performed in Section V. Finally, Section VI concludes this article.

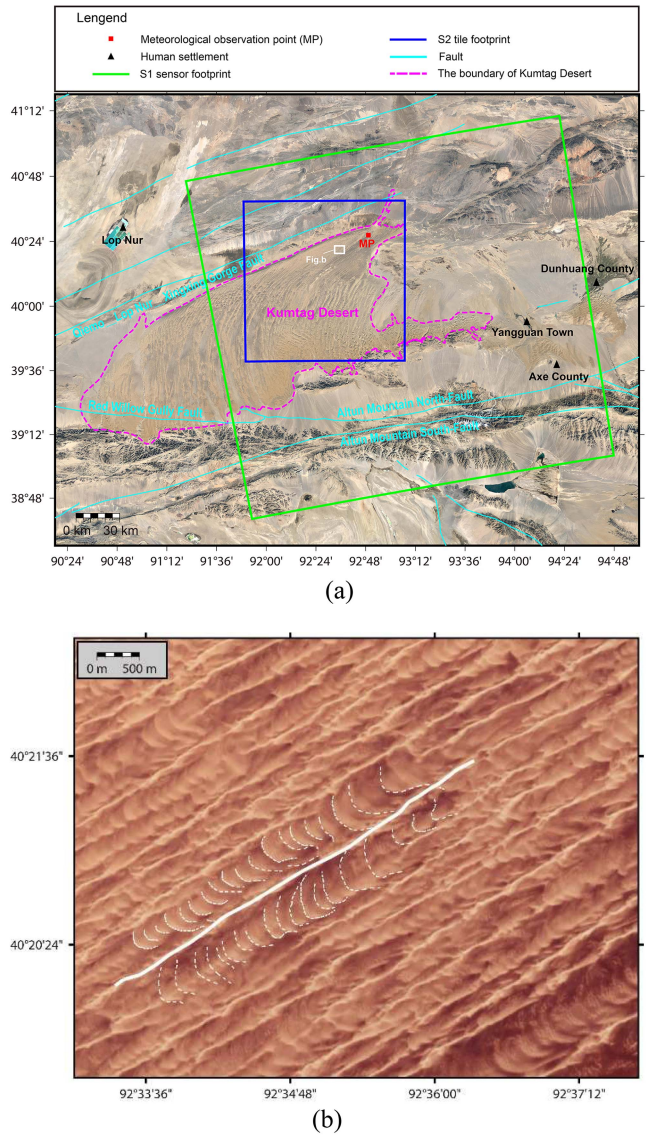

Fig. 1. (a) Geographical background of the Kumtag Desert, combined with the image coverages of Sentinel-1 (S1) and Sentinel-2 (S2). (b) Enlarged view on the geomorphological structure of the feather-shaped dunes in Kumtag Desert, in which the solid white line denotes the pinna rachis of the feather-shaped dunes constructed by the longitudinal barchan bridges, and the dotted white lines indicate the rami of the feather-shaped dunes constructed by the cambered transverse dunes.

II. Study Region and Datasets

A. Study Region

The Kumtag Desert is well-known as the "dry pole" of Eurasia with an average of annual precipitation below 30 mm/year and an annual difference in air temperature from −8 °C to 28 °C [35]. Located in the south side of the Lop Nur lowland in the Xinjiang Autonomous Region and the north of the Altun Mountain [see Fig. 1(a)], the Kumtag Desert is the Chinese fourth largest mobile desert covering an area of approximately 23 000 km^2 [36]. Not until 2007 year that the Chinese Government organized a large-scale scientific expedition project, there is not a systematic understanding of the geological and geomorphological aspects

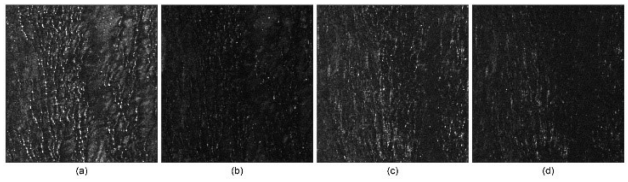

Fig. 2. S1 VV polarization images of (a) path 70, frame 1312 (ascending) acquired at January 6, 2021; (b) path 143, frame 126 (ascending) acquired at January 11, 2021; (c) path 48, frame 459 (descending) acquired at January 4, 2021; and (d) path 150, frame 461 (descending) acquired at January 11, 2021.

of the mobile desert in geoscience community. Bordered by the western famous city of Dunhuang, the Kumtag Desert is a key pathway for the ancient "Silk Road" and occupies an important choke position in the Chinese National Development Strategy of "One Belt, One Road." Notably, the desert is the home of the rare feather-shaped dunes [see Fig. 1(b)] in China [37], [38], whose causation is still fascinating and explored by the scientific community [34], [39]. Due to the complex topography and windy weather, Kumtag Desert occupied 90% of active dunes in the interior and thus has been vividly named as the "Sand River" in those historical classics [40].

B. Remote Sensing Observation Datasets

Launched from the year of 2015 by the European Space Agency (ESA), the S2 optical observation mission constructed by two A-B satellites was used. Totally, as shown in Table S1, 63 images of S2 (T46TDK) imaged from September 7, 2016 to October 16, 2022 were collected here. According to Ding et al. [20], the near-infrared band with higher radiometric performance than other 10-m bands of S2 were selected to quantify the dune migration in Kumtag Desert.

Comparatively, with the similar dual-satellites of A-B constellation configuration, the C-band SAR S1 mission of ESA is also used to detect and quantify the mobility of the feather-shaped dunes. There are totally four satellite footprints covering the Kumtag Desert. However, with the cross-comparison of four different image coverages in Fig. 2, the strongest echoed signals of the feather-shaped dunes can be clearly identified in the image coverage of Path 70, Frame 1312, ascending direction in single-polarization VV channel. As displayed in Table S1, a total of 176 S1 images for this image coverage of Path 70, Frame 1312, ascending direction thus were utilized to extract the slant-range/azimuth dune displacement velocity. Detail parameter configurations for S2 and S1 are demonstrated in Table S2 and Tables I and II, respectively.

C. Meteorological Datasets

To further validate these remote sensing results, the wind observation datasets of the Meteorological Observation Point of MP [see Fig. 1(a)], from 2015 to 2022, were obtained from NASA's official website (https://power.larc.nasa.gov/data-access-viewer/), and subsequently were utilized to calculate the drift potential (DP) for evaluating the activity of sand transport [41]. As displayed in Fig. 3, assuming the threshold of

TABLE I
PARAMETER CONFIGURATION FOR SENTINEL-1 (S1) OFFSET-TRACKING PROCESSING

Sensor	S1
Multilooks in range (pixels)	20
Multilooks in azimuth (pixels)	4
Spatial baseline thresholds (m)	[0, 100]
Temporal baseline thresholds (days)	[25, 60]
Correlation window size [range, azimuth] (pixels)	[128, 128]
Cross-correlation thresholds	0.1

TABLE II
PARAMETERS CONFIGURATION USING FOR S1 SBAS–INSAR PROCESSING

Sensor	S1
Multilooks in range (pixels)	20
Multilooks in azimuth (pixels)	4
Spatial baseline thresholds (m)	[0, 220]
Temporal baseline thresholds (days)	[12 108]

wind speed blowing the sands up as around 5 m/s in Kumtag Desert [37], the yearly total DP value maintains approximately 531.71 VU, and belongs to a high energy level of wind power. The resultant drift potential (RDP) value is approximately 359.13 VU in a sand drift direction of around 259.58°. The directional variability (RDP/DP) value with a range of [0–1] is approximately 0.63, indicating the directional complexity of potential dune mobility.

Additionally, with a grid resolution of 0.1° × 0.1° acquired from the Global Precipitation Measurement Mission, the dataset of daily precipitation observation is downloaded from https://developers.google.com/earthengine/datasets/catalog/NASA_GPM_L3_IMERG_V05, and then utilized to indicate the water content of the study region. Analysis on these precipitation observations showed that the average precipitation of MP maintained around 30 mm/year in the level of extremely drought, and meanwhile the maximal rainfall was concentrated in the windy summer months.

D. Topographic Datasets

To better analyze the relationship between the topographic relief and the migration rates of the feather-shaped dunes, the DEM dataset of this study area was required. According to Blumberg [25], the DEM generated by X-band sensor with a shorter radar wavelength than C-band is more sensitive to a smaller scale ripple undulation of dunes' surface and thus can better reveal out the elevation of the feather-shaped dunes. Hence, rather than the conventional SRTM-C DEM, the TanDEM-X DEM in a spatial resolution of approximately ∼90 m (applied from https://download.geoservice.dlr.de/TDM90/) was used here to analyze the coupling relationship between the local topography

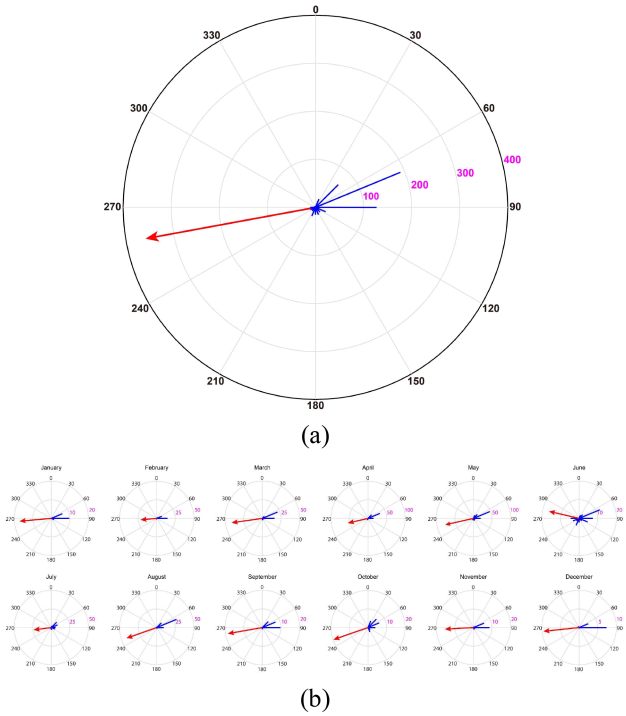

Fig. 3. (a) Sand rose of the meteorological observation point of MP in the sand source region of Kumtag Desert, in which the blue line and red arrow denote the sand drift potential (DP) and the resultant sand drift potential (RDP), respectively. (b) Average DP (blue lines) and RDP (red arrows) of each month from January to December for a whole year.

and the movements of feather-shaped dunes. This dataset was collected by two identical X-band SAR satellites flying in adjacent orbits over the period of 2010–2015, more closed to the observation temporal span of S1 and S2 datasets compared to the SRTM-C DEM generated in 2000.

III. METHODOLOGY

As detailed in Fig. 4, the methodology was divided into five subsections as follows: 1) quantification of dune migration, including the optical image selection, the cross-correlation processing, and the noise suppression, were described in Section II-I-A; 2) similarly, measuring the dune movements in slant-range and azimuth directions with SAR offset-tracking was described in Section III-B; 3) the mathematical models for inverting the East–West (EW)/North–South (NS), and slant-range/azimuth displacement time series from the optical and SAR observations were detailed in Section III-C; 4) the SBAS-InSAR technique was used to detect active regions and quantify the line-of-sight (LOS) displacement in Section III-D; (5) the InSAR coherence time series were used to evaluate the activity of the feather-shaped dunes in Section III-E; and 6) the 3-D displacement velocities of the feather-shaped dunes were extracted from the optical and SAR-derived results in Section III-F.

A. Optical Image Cross-Correlation

Once the L1C-level orthorectification products of S2 images have been retrieved, there are three main processes to be performed: image selection, image coregistration, cross-correlation

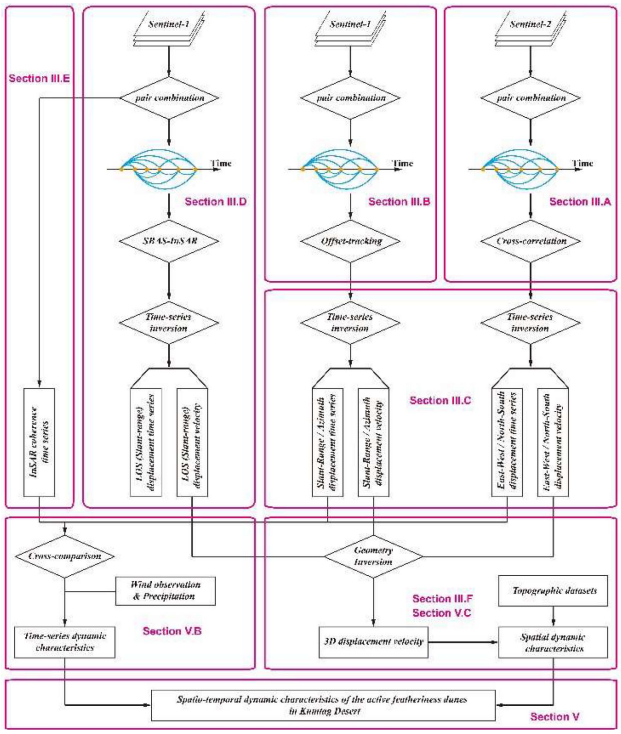

Fig. 4. Overview of the methodology proposed for investigating the multi-dimensional dynamic characteristics of the feather-shaped dunes in Kumtag Desert.

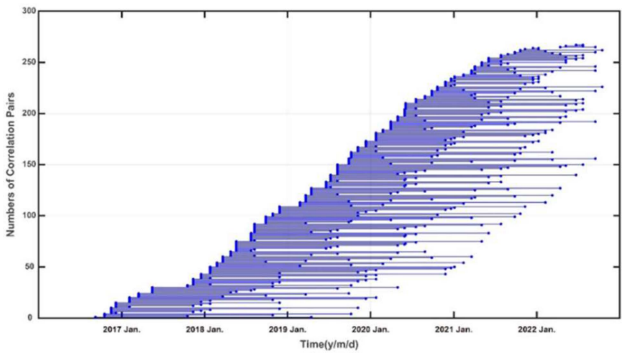

Fig. 5. Image pairing networks of the S2 observations that are used for the optical image cross-correlation.

processing, and noise suppression. Following the image pairing strategy of Ding et al. [20], Table S2 shows the detail baseline thresholds configured in this article.

Other than the baseline parameters, the specific parameters of search window size, search steps, frequency mask, and iterations were configured in accordance with the COSI-CORR Users' Guide 2015 [42] and detailed in Table S2. As shown in Fig. 5, a total of 267 groups of S2 image pairs were used for image correlation. Assuming the number of S2 images is $M^{\text{corr}}+1$, afterwards N^{corr} pairs of optical image cross-correlation measurements in the EW and NS components can be generated using the COSI-Corr batch-processing procedure. Each group of optical image cross-correlation measurements $\delta d_j^{\text{corr}} (j = 1, \ldots, N^{\text{corr}})$ in either EW or NS direction can be

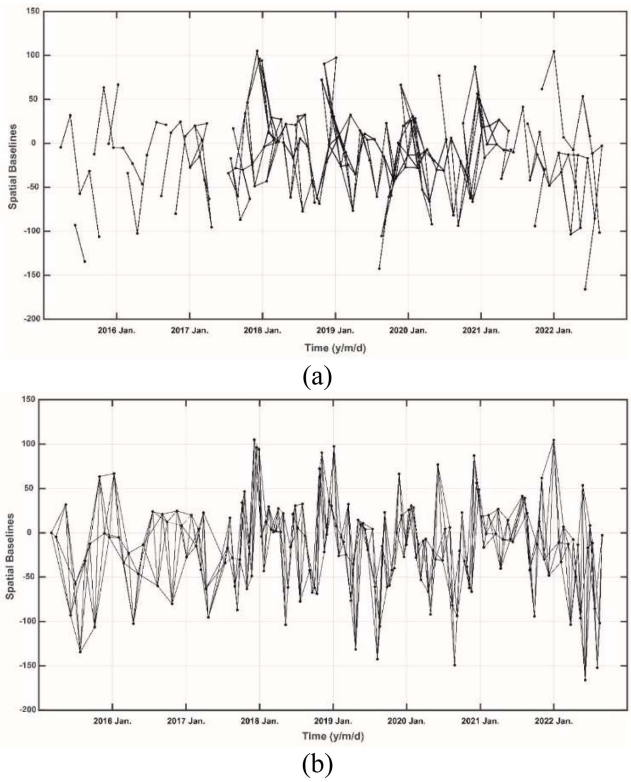

Fig. 6. Spatial and temporal baseline networks of (a) S1 images using for the pixel offset tracking processing, and (b) S1 observations that are used for the SBAS–InSAR processing.

indicated as

$$\sum_{i=s_j+1}^{m_j} \left(t_i^{\text{corr}} - t_{i-1}^{\text{corr}}\right) v_i^{\text{corr}} = \delta d_j^{\text{corr}} \ (j = 1, 2, \ldots, N^{\text{corr}}) \tag{1}$$

where $t_{m_j}^{\text{corr}}$ and $t_{s_j}^{\text{corr}}$ denote the acquisition times of the master S2 image and the slave S2 image for each pixel, respectively. The variable of $v_i^{\text{corr}} (i = 1, 2, \ldots, M^{\text{corr}})$ represent the average offset velocity calculated between consecutive S2 acquisitions. As the noise $\delta\Delta_j^{\text{corr}}$ in the correlation vector is corrected by the postprocessing routines [43], (1) has the variant as follows:

$$\sum_{i=s_j+1}^{m_j} \left(t_i^{\text{corr}} - t_{i-1}^{\text{corr}}\right) v_i^{\text{corr}} = \delta d_j^{\text{corr}} - \delta\Delta_j^{\text{corr}} \ (j = 1, 2, \ldots, N^{\text{corr}}). \tag{2}$$

B. SAR Offset-Tracking

When the dune slope is approximately perpendicular to the radar signal, a dihedral, trihedral, or even multisided structure with strong scattering characteristics will be formed. Thus, limited by the spatial characteristics of specific dune forms and imaging geometry of radar satellites, the reflected signal in the radar image will be extremely obvious and appear as the bright points with high backscattering signals (see Fig. 2). As a conventional technique of measuring the movements of these

feature points between two images by performing the patch intensity cross-correlation optimization, SAR offset-tracking has been widely used in the estimation of ground dynamic events (earthquakes, landslides, glaciers, etc.). However, the successful cases of quantifying the dune migration with SAR offset-tracking were scarce in recent literatures. By performing the offset-tracking on S1 amplitude time-series images, the text in this part will attempt to perform multitemporal tracking and offset measurement on these strong scattering points, and then quantify the dune movements along the slant-range and azimuth directions in radar imaging coordinate system. More technical processing sequence for offset-tracking can be found in Text S1 of the Supplementary file and the specific parameters were detailed in Table I. Subsequently, with the constricts of these parameters, a total of 264 SAR image pairs constructed by 170 SAR images were selected as displayed in Fig. 6(a).

Suppose the number of S1 images for offset-tracking processing is $M^{\mathrm{OT}}+1$, then N^{OT} pairs of SAR offset-tracking measurements in two components of slant-range and azimuth can be acquired. With the similar rationale for the S2 image cross-correlation processing, the linear mathematical model linking the acquisition time of master image $t^{\mathrm{OT}}_{m_j}$ and slave image $t^{\mathrm{OT}}_{s_j}$, the mean offset velocity v^{OT}_i $(i=1,2,\ldots,M^{\mathrm{OT}})$, the SAR offset-tracking measurements $\delta d^{\mathrm{OT}}_j (j=1,2,\ldots,N^{\mathrm{OT}})$ in slant-range or azimuth direction, and the noise $\delta\Delta^{\mathrm{OT}}_j$ in the calculated offset vector can be constructed following Casu et al. [44] as

$$\sum_{i=s_j+1}^{m_j}\left(t^{\mathrm{OT}}_i - t^{\mathrm{OT}}_{i-1}\right)v^{\mathrm{OT}}_i = \delta d^{\mathrm{OT}}_j - \delta\Delta^{\mathrm{OT}}_j \ \left(j=1,2,\ldots,N^{\mathrm{OT}}\right). \tag{3}$$

C. Two-Dimensional Displacement Inversion

Here, the time-series inversion methods with S2 image cross-correlation and S1 offset-tracking results were conjointly detailed as follows. For the S2 image cross-correlation, as described in Section III-A, (2) can be simplified into (4), in which the element located at $[j,i]$ $(s^{\mathrm{corr}}_j+1\le i\le m^{\mathrm{corr}}_j, j=1,2,\ldots,N^{\mathrm{corr}})$ of matrix B^{corr} is $(t^{\mathrm{corr}}_i - t^{\mathrm{corr}}_{i-1})$ and the other elements are zero

$$B^{\mathrm{corr}}\,v^{\mathrm{corr}} = d^{\mathrm{corr}} - \Delta^{\mathrm{corr}}. \tag{4}$$

The optical-derived displacement velocities v^{corr} of every observation interval subsequently is inverted in the least-square sense as shown in (5). It is worth noting that P^{corr} is the matrix weighting the correlation results. The optical-derived EW/NS displacement time series D^{corr}_m and the average displacement velocity $\bar{v}^{\mathrm{corr}}$ finally are derived as follows:

$$v^{\mathrm{corr}} = \left[\left(B^{\mathrm{corr}}\right)^T P^{\mathrm{corr}} B^{\mathrm{corr}}\right]^{-1}\cdot\left(B^{\mathrm{corr}}\right)^T P^{\mathrm{corr}}\cdot\left(d^{\mathrm{corr}}-\Delta^{\mathrm{corr}}\right) \tag{5}$$

$$D^{\mathrm{corr}}_m = \begin{cases} 0 & (m=1) \\ \sum_{i=1}^{m-1} v^{\mathrm{corr}}_i t^{\mathrm{corr}}_i & (m=2,\ldots,n) \end{cases} \tag{6}$$

$$\bar{v}^{\mathrm{corr}} = \sum_{i=1}^{n-1} v^{\mathrm{corr}}_i \Delta t^{\mathrm{corr}}_i \Big/ \sum_{i=1}^{n-1}\Delta t^{\mathrm{corr}}_i. \tag{7}$$

With the similar time-series inversion rationale of the optical image cross-correlation measurements, the SAR-derived slant-range and azimuth displacement velocities v^{OT}, cumulative displacement time series D^{OT}_m, and the average displacement velocity $\bar{v}^{\mathrm{OT}}$ will be retrieved as follows:

$$v^{\mathrm{OT}} = \left[\left(B^{\mathrm{OT}}\right)^T P^{\mathrm{OT}} B^{\mathrm{OT}}\right]^{-1}\cdot\left(B^{\mathrm{OT}}\right)^T P^{\mathrm{OT}}\cdot\left(d^{\mathrm{OT}}-\Delta^{\mathrm{OT}}\right) \tag{8}$$

$$D^{\mathrm{OT}}_m = \begin{cases} 0 & (m=1) \\ \sum_{i=1}^{m-1} v^{\mathrm{OT}}_i t^{\mathrm{OT}}_i & (m=2,\ldots,n) \end{cases} \tag{9}$$

$$\bar{v}^{\mathrm{OT}} = \sum_{i=1}^{n-1} v^{\mathrm{OT}}_i \Delta t^{\mathrm{OT}}_i \Big/ \sum_{i=1}^{n-1}\Delta t^{\mathrm{OT}}_i. \tag{10}$$

It is worth noting that when the coefficient matrix B^{corr} or B^{OT} is rank-deficient, such as the spatiotemporal baseline network for S2 or S1 is not continuous, the method of singular value decomposition (SVD) is utilized to retrieve the least-square solutions of displacement velocities [20], [44]. The similar technical details of SVD method for SBAS-InSAR are illuminated in Section III-D.

D. SBAS-InSAR

The SBAS-InSAR is a traditional multitemporal processing technique that has been widely used to measure the ground displacements along the radar's LOS direction. To test the applicability of traditional InSAR technique, the SBAS-InSAR was also used to retrieve the dune displacement fields of Kumtag Desert in this article. The detail parameters of SBAS-InSAR can be found in Table II. Finally, as displayed in Fig. 6(b), there are a total of 522 InSAR pairs constructed by 176 SAR images that were selected for deriving the displacement time series with the strategy as follows.

Suppose the number of S1 images using for InSAR processing is $M^{\mathrm{los}}+1$, then N^{los} pairs of InSAR measurements can be retrieved. The linear mathematical model of linking the acquisition times of the master $t^{\mathrm{los}}_{m_j}$ and the slave $t^{\mathrm{los}}_{s_j}$, the mean offset velocity v^{los}_i $(i=1,2,\ldots,M^{\mathrm{los}})$ between adjacent S1 acquisitions, the InSAR measurements $\delta d^{\mathrm{los}}_j$ $(j=1,\ldots,N^{\mathrm{los}})$, and the noise $\delta\Delta^{\mathrm{los}}_j$ can be illuminated as follows:

$$\sum_{i=s_j+1}^{m_j}\left(t^{\mathrm{los}}_i - t^{\mathrm{los}}_{i-1}\right)v^{\mathrm{los}}_i = \delta d^{\mathrm{los}}_j - \delta\Delta^{\mathrm{los}}_j \ \left(j=1,2,\ldots,N^{\mathrm{los}}\right). \tag{11}$$

This formula also can be simplified as follows:

$$B^{\mathrm{los}}\,v^{\mathrm{los}} = d^{\mathrm{los}} - \Delta^{\mathrm{los}}. \tag{12}$$

The B^{los} is a diagonal matrix, in which the value located at $[j,i]$ $(s^{\mathrm{los}}_j+1\le i\le m^{\mathrm{los}}_j, j=1,2,\ldots,N^{\mathrm{los}})$ of its diagonal

is $(t_i^{\text{los}} - t_{i-1}^{\text{los}})$. Under the normal conditions, if B^{los} is a nonsingular matrix, the least-square solution of v^{los} can be retrieved through (13). Nevertheless, when B^{los} is rank-deficient, the SVD method [45] can be utilized to derive the least-square solution of v^{los}, displayed as follows:

$$v^{\text{los}} = \left[\left(B^{\text{los}}\right)^T B^{\text{los}}\right]^{-1} \cdot \left(B^{\text{los}}\right)^T \cdot \left(d^{\text{los}} - \Delta^{\text{los}}\right) \tag{13}$$

$$B^{\text{los}} = U^{\text{los}} \left(S^{\text{los}}\right)^{+} \left(V^{\text{los}}\right)^T. \tag{14}$$

E. InSAR Coherence Time Series

An assessment of the quality of InSAR measurements is often made using coherence [46], which provides a measure of the similarity of SAR echo signals. Coherence values distribute from 0 to 1, high values of which generally represent the high coherence in InSAR measurements. A coherence-estimated window of 20 $\times$ 4 pixels in the slant-range and azimuth direction is chose here to calculate the coherence values following the methods detailed in Text S2 of the Supplementary file.

The coherence γ was conventionally influenced by the spatial baseline, the temporal baseline, and other factors (such as the thermal noise, misregistration, and atmospheric effects). In this article, the spatial baselines of SAR image pairs maintained from 0 to 220 m [see Fig. 6(b)] that were small and similar enough corresponding to a spatial decorrelation of approximately constant. In other words, the spatial coherence noise poses a negligible impact on the evolution of temporal coherence. Thus, ignoring the factors of small spatial baseline, thermal noise, misregistration, and atmospheric effects, the temporal coherence triggered by the environmental changes over time can be indicated by the total coherence value of γ. To better evaluate the dune mobility and sand transport of the region of interest (ROI) in a large-scale (dune-field scale) level, an index of change detection (ICD) was designed as

$$\text{ICD} = \text{Ave}\ (\gamma) \tag{15}$$

where the Ave (γ) is the average of the coherence value γ of the ROI. Generally, the larger ICD indicates a lower dune mobility, and the smaller ICD indicates a higher dune mobility.

F. 3-D Displacement Extraction

As aforementioned in Section III-C, the displacements in the EW/NS directions of optical coordinate system and the slant-range/azimuth directions of SAR coordinate system are extracted. Additionally, as depicted in Section III-D, if the dune morphology does not change much, the SBAS-InSAR can acquire the sparse displacements along the radar's LOS direction, in consistent with the slant-range direction. Because of the differences in the error level of optical and SAR-derived displacements, it is of great significance to reasonably integrate these displacement signals in different spatial dimensions to obtain the accurate 3-D displacement velocity of the feather-shaped dunes.

Considering the systematic offsets existed between the optical and SAR image coordinate systems, the coregistration procedure should be performed. For the first step, the SAR-derived displacement results were transformed into the projection in consistent to the optical results with the same resolution following the cubic convolution resampling strategy. Subsequently, the resampling SAR offset-tracking results were coregistered with the optical results. After eliminating the misalignments within different sensors, the coordinate system of SAR/optical results were consistent and then can be used for the retrieval of 3-D dune displacement velocity. Considering the dependence between the radar and the optical displacement measurements, the radar-derived displacements can be used to restrict the optical 2-D displacement measurements, and then solve the real 3-D displacement velocity of the feather-shaped dunes, following the mathematical relationship depicted as follows:

$$\begin{bmatrix} v_{\text{los}} \\ v_{\text{sr}} \\ v_{\text{ew}} \\ v_{\text{ns}} \end{bmatrix} = \begin{bmatrix} -\cos\theta & \cos\alpha \cdot \sin\theta & \sin\alpha \cdot \sin\theta \\ -\cos\theta & \cos\alpha \cdot \sin\theta & \sin\alpha \cdot \sin\theta \\ 0 & 1 & 0 \\ 0 & 0 & 1 \end{bmatrix} \begin{bmatrix} v_{\text{vert}} \\ v_{\text{east}} \\ v_{\text{north}} \end{bmatrix}. \tag{16}$$

This formula represents the geometric relationship between the theoretical 3-D displacement velocity and the SAR-/optical-derived displacement velocities. Among them, α represents the flighting angle clockwise calculated from the due North direction, and θ represents the incidence angle. v_{los} represents the InSAR-derived LOS displacement velocities, and v_{sr} represents the slant-range displacement velocities acquired by SAR offset-tracking. v_{ew} and v_{ns} represent the EW and NS displacement velocities derived from the optical images, respectively. v_{vert}, v_{east}, and v_{north} represent the inverted displacement velocities in the vertical, EW, and NS directions, respectively. Taking the dune displacement measurements extracted from the optical and SAR images as two types of observations, the displacement velocity in each type of observation can be estimated with the theory of least-square adjustment. Besides, to better constrict the disparities in accuracy of different techniques, the involved measurements were weighted with the reciprocal of standard deviation (STD) in the stable area when performing the least-square inversion.

As aforementioned above, to retrieve the 3-D displacement velocities, the constraints of multisensors' measurements were crucial for the reasonable fusion of the dune displacements. For example, the measurements acquired by the SBAS-InSAR can identify and suppress the possible large measurement bias for the SAR offset-tracking or optical image cross-correlation in relatively inactive region. Besides, the vertical displacements can only be derived from the SAR slant-range offset-tracking and SBAS-InSAR measurements, with the constraints of the horizontal measurements derived from the optical image cross-correlation. Thus, the measurement precision of the vertical displacement velocity may be relatively higher than the EW/NS displacements conjointly inverted from the optical- and SAR-derived measurements.

IV. Evaluation and Validation

Following the methodology of Section III, corresponding precision evaluation and comparison were discussed as follows.

A. Precision Evaluation for Single Sensor

Before performing the temporal analysis, the measurement uncertainties of the optical- and SAR-derived displacement velocity and time series were evaluated here. As displayed in Figs. S2–S3, the measurement uncertainties indicated by the measurements' STD for the stable or nonactive dune region of optical cross-correlation results vary from 0.70 (EW)/0.68 (NS) m to 1.56 (EW)/1.70 (NS) m with the average of around 1.20 (EW)/1.28 (NS) m for S2 after inversion. Comparatively, the measurement uncertainties of SAR offset-tracking results in slant-range/azimuth vary from 0.01 (slant-range)/0.04 (azimuth) m to 0.08 (slant-range)/0.20 (azimuth) m with the average of around 0.03 (slant-range)/0.07 (azimuth) m for S1 after inversion. Similarly, for each component, the difference of the STD before and after inversion is estimated. On average, the time-series inversion provides the improvements of approximately 78% (EW)/77% (NS) for S2 and approximately 12% (slant-range)/20% (azimuth) for S1, respectively.

For the optical-derived horizontal displacement results, the uncertainty (STD) is averagely 2.32 $\pm$ 0.24 m, denoting approximately 1/25 pixels of the grid resolution defined by the search step of correlation window. Specifically, STDs of the optical-derived displacement results distribute from 1.15 to 1.77 m (EW)/1.24 to 2.07 m (NS) with mean values of approximately 1.55 $\pm$ 0.15 m (EW)/1.72 $\pm$ 0.19 m (NS). The uncertainty in NS components was slightly larger than that in EW components, possibly because of the different noise levels of topographic shadowing artifacts in two components. Comparatively, STDs of the SAR offset-tracking displacement time series distribute from 0.02 to 0.31 m (slant-range)/0.09 to 0.43 m (azimuth) with the mean values of approximately 0.14 $\pm$ 0.06 m (slant-range)/0.31 $\pm$ 0.07 m (azimuth).

B. Comparison Between Different Sensors

A comparison of the measurement consistency for different sensors (S2 vs. S1) should also be made before inverting the multidimensional dynamic characteristics with the optical and SAR observations. This comparison can be performed by quantifying the statistical indexes of the spatiotemporally superimposed stable areas of the optical-derived EW/NS displacement velocities, the slant-range/azimuth displacement velocities of SAR offset-tracking, and the LOS displacement velocities of SBAS-InSAR. Specifically, assuming the real values of the inactive dune region inside the Kumtag Desert were zero, the measurements derived from the optical image cross-correlation, the SAR offset-tracking, and the SBAS-InSAR were compared to evaluate the measurement consistency. As shown in Fig. 7, inside the Kumtag Desert, the InSAR measurements present invalid decorrelation noise in the active dune region and present as mini-values closed to zero in the inactive dune region. These measurements in the inactive dune region of three different techniques were displayed in Table III. The measuring precision of the SBAS-InSAR technique closed to zero was higher than the other two approaches.

Comparatively, the measurement precision of SAR offset-tracking was commonly two folders higher than that of optical image cross-correlation. Thus, the sensibility of these three techniques on detecting ground changes was SBAS-InSAR > SAR offset-tracking > optical image cross-correlation, respectively. However, as an active aeolian activity in Kumtag Desert, the movements of the feather-shaped dunes generally possess large displacement gradients (*several meters* level) out of the measuring capability of SBAS-InSAR (*millimeter–centimeter* level) and even SAR offset-tracking (*decimeter–meter* level). In other words, the capability of quantifying the dune migration with the large displacement gradients was optical image cross-correlation > SAR offset-tracking > SBAS-InSAR, respectively. These differences were mainly caused by the imaging radiometric disparities (optical versus SAR) for different sensors and the variation of measuring sensitivity (amplitude versus phase) for different techniques. Conventionally, with a larger quantization

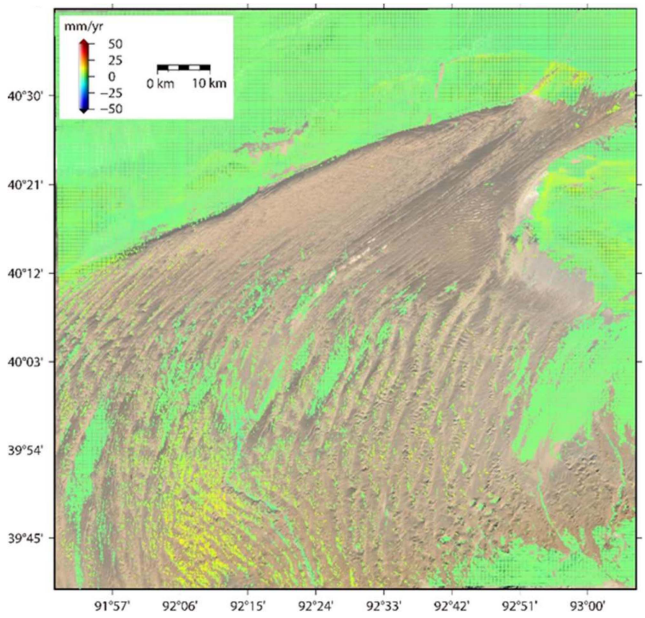

Fig. 7. SBAS–InSAR derived dune displacement velocity (mm/year) along the line-of-sight (LOS) direction with lots of decorrelation region induced by the large dune morphology changes and the low dielectric constants.

TABLE III
CROSS-COMPARISON OF MEASUREMENT UNCERTAINTY INDICATED BY THE AVERAGE AND THE STANDARD DEVIATION (STD) BETWEEN DIFFERENT TECHNIQUES

Items	Optical image cross-correlation		SAR offset-tracking		SBAS-InSAR
	EW	NS	Slant-range	Azimuth	LOS
Average (10^{-2} *m/year)	−22.12	−9.44	−9.63	3.69	0.13
STD (10^{-2} *m/year)	100.92	134.32	65.02	74.00	0.24

mechanism compared to the SAR sensor, the optical sensor can capture more ground reflector signals illuminating the surface texture on the dune surface. Even though conjointly possessing the phase and amplitude signals, the strong absorbing ability on the radar wave of sand grains and the deficiency in the specific dune structures with strong radar echoes weaken the effective information in SAR images for quantifying the dune movements. Besides, the configuration of the smaller search window size of the optical sensor compared to the SAR sensor was also another factor triggering this disparity in measurements.

Additionally, as displayed in Fig. S3 and Table S4, the comparison on the dune migration rates derived from the manual digitization with historical Google™ Earth images and this article demonstrates a high measurement consistency.

V. Result and Discussion

By interpreting the displacement results, the feasibility of combing SAR and optical techniques to identify and quantify dune mobility, and the temporal and spatial dynamic evolution characteristics of feather-shaped dunes were discussed in following subsections, respectively.

A. Feasibility of Combining SAR and Optical Techniques to Identify and Quantify Dune Mobility

With respect to the previous articles and test results, the SAR observations (especially for InSAR technique) were considered not suitable for quantifying the dune movements (see Fig. 7), due to the weak radar echoes caused by unfavorable imaging characteristics, such as the low dielectric constants and the changeable dune morphology. Thus, there are deficient studies on the quantification of dune movements with SAR observations. However, the specific dune structure/geometry and less-changeable dune forms for the peculiar feather-shaped dunes in Kumtag Desert present stronger radar reflector signals, which can be clearly identified in SAR images. Maintaining the magnitude of several meters, the morphological movements of the feather-shaped dunes have extended beyond the monitoring capability of traditional InSAR techniques. To overcome these technical defects, the SAR offset-tracking suitable for measuring the large ground displacement gradients were used to quantify the dune movements with these points with strong scattering strength in SAR images (see Fig. 8). Comparatively, the optical image cross-correlation has been validated as efficient in capturing the horizontal displacement velocity of dune migration (see Fig. 9).

With the methodology of detecting the active dune region as depicted in Ding et al. [20], the area of active dunes in Kumtag Desert can be derived. As shown in Fig. 10, the area of active dune region detected through the optical image cross-correlation is around 2649.1 km^2, compared to that detected by SAR offset-tracking of around 2187.1 km^2. Furthermore, the area of active dune region consistently detected by the optical and SAR techniques was around 1350.8 km^2. As presented in Figs. 7 and 8, it is found that optical image cross-correlation can detect finer details and larger area of active dune fields than the SAR offset-tracking. The reason can be illuminated

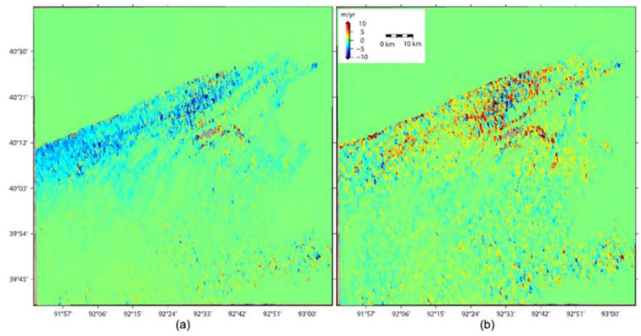

Fig. 8. (a) Slant-range and (b) azimuth displacement velocities (m/year) of the feather-shaped dunes in Kumtag Desert with a geocoding spatial resolution of around 71.0 m (EW) × 46.3 m (NS) derived from the S1 SAR ascending observations. The positive values in (b) denotes the reverse direction of the flighting direction of the S1 SAR sensor, as shown in Fig. S1.

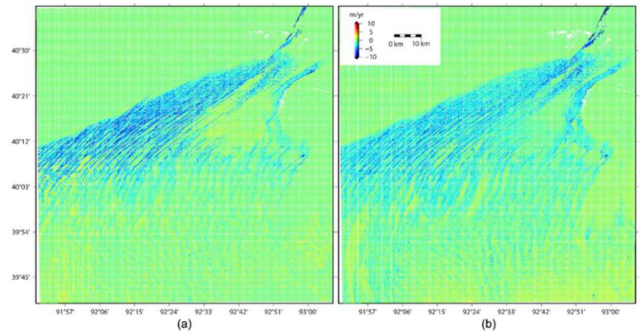

Fig. 9. (a) EW and (b) NS dune migration velocities (m/year) with a geocoding spatial resolution of around 60 m (EW) × 60 m (NS) derived from the S2 optical satellite observations.

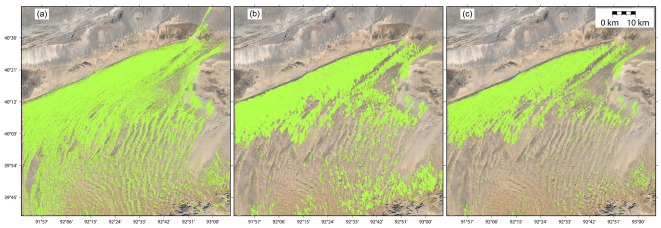

Fig. 10. Active dune region detected by (a) optical image cross-correlation, (b) SAR pixel offset-tracking, and (c) intersection of the optical and SAR techniques.

as the smaller search window size configured in optical image cross-correlation than SAR offset-tracking, and the richer scene texture of optical images than SAR images.

Besides, limited by the specific ascending flighting direction perpendicular to the dune migration direction and coarser resolution, the azimuth-oriented measurements of SAR offset-tracking showed a consistent measurement tendency with respect to the optical-derived NS displacements. However, the measurement noise in the SAR-derived slant-range/azimuth was larger than the optical-derived results, especially for the azimuthal measurements due to the coarser resolution of SAR image in the azimuth orientation. Thus, the SAR-derived azimuthal measurements were not considered in inverting the local vertical displacement characteristics. As presented in Fig. 9, the optical

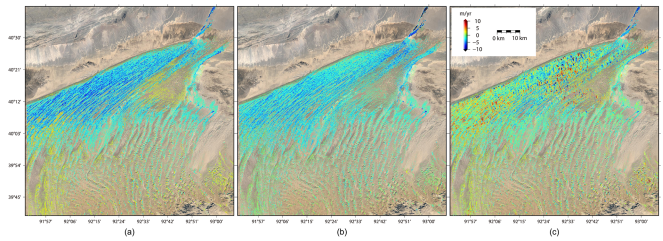

Fig. 11. 3-D displacement velocity (m/year) derived jointly by the optical image cross-correlation (EW and NS), the SAR ascending image offset-tracking (only considering the slant-range result), and the SBAS–InSAR measurements (only considering the efficient measurements inside the desert). The negative values in (a)–(c) denote the dune displacements occurred along the direction of (a) West, (b) South, and (c) subsidence, respectively, vice versa.

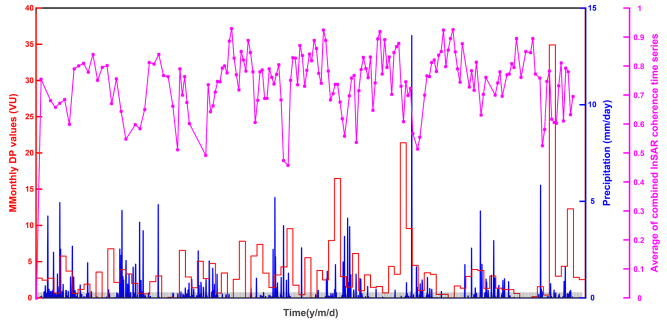

Fig. 12. Comparison between the local precipitation, the monthly DP values, and the InSAR coherence time series. High negative correlation between the coherence values and the precipitation can be easily identified, denoting the coherence values of InSAR technique maybe interfered by the soil water content.

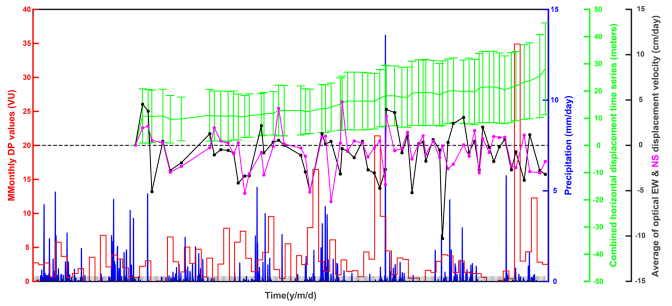

Fig. 13. Horizontal cumulative displacement time series (average ± STD) and velocity time series of two components (EW and NS) for the whole optical-derived measurements of dune migration in Kumtag Desert. The optical-derived results were also compared to the local precipitation and the monthly DP values.

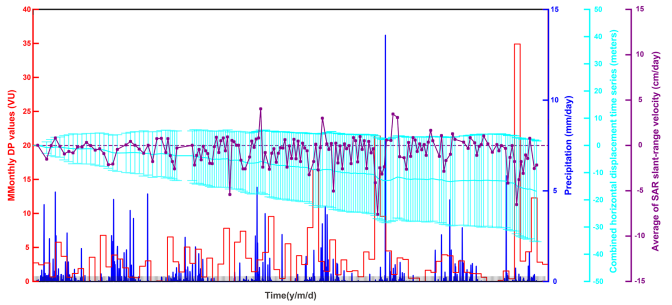

Fig. 14. Cumulative slant-range displacements (average ± STD) and velocity time series for the whole SAR offset-tracking measurements of dune migration in Kumtag Desert. The SAR offset-tracking results were also compared to the local precipitation and the monthly DP values.

image cross-correlation can directly provide the EW and NS displacement velocity. Then, the 3-D displacement inversion can be performed with the optical- and SAR-derived results, as displayed in Fig. 11.

B. Temporally Dynamic Evolution Patterns of Feather-Shaped Dunes

As an effective way for measuring the sand transport in the study community of desert science, DP was a conventional index to indicate the morphological changes of mobile dunes [41]. In the generic sense, the small DP values represent the subtle geomorphological changes, vice versa. Therefore, DP was utilized in this article to validate these results derived from the optical and SAR observations. Except for the DP, the InSAR coherence was also utilized to indicate the temporal evolution of the changeable dune morphology. As shown in Fig. 12, the InSAR coherence time series present as a dominant seasonal evolution with the high coherence values mainly concentrated in the windy and rainy seasons (spring and summer months), and the low coherence values mainly in the less-windy and arid seasons (autumn and winter months). As is well-known to us, the high soil humidity may trigger the loss of InSAR coherence. However, with respect to the specific climatic features of low precipitation and high evaporation capability inside the Kumtag Desert, the wind condition was considered as the dominant trigger factor of controlling the temporal changes of InSAR coherence for measurements on the mobile feather-shaped dunes.

As displayed in Figs. 13 and 14, an obvious enhancement in dune migration velocity after March 21, 2022 was simultaneously observed in the optical-derived horizontal and SAR-derived slant-range displacement time series. Also, a dominant enhancement on DP values indicating a large wind energy was observed on May, 2022, in consistency with the rapid increment of dune displacement time series. Generally, the dune dynamic mechanism was comparatively complex due to the fickle wind conditions, directly causing the changeable migration of these feather-shaped dunes in the EW/NS directions (see Fig. 13). As displayed in Figs. 13 and 14, the high correlation between the wind DP values and the optical-/SAR-derived dune migration velocities can be easily identified.

C. Spatially Dynamic Evolution Patterns of Feather-Shaped Dunes

The frequency distribution of the horizontal EW/NS displacement component of the derived 3-D displacement velocity is displayed in Fig. 15. It is worth noting that the feather-shaped dunes predominantly move along the northeastern–southwestern orientation ($204.32° \pm 52.15°$) with the rates of 3.34 ± 2.26 m/year within the study region, which is highly correlated with the predominant wind conditions as displayed in Fig. 3. Furthermore, it is worth noting that the predominant direction of dune migration was similarly perpendicular to the flighting azimuth direction and parallel to the slant-range direction of the S1 sensor. Thus, the specific dune formation and migration direction

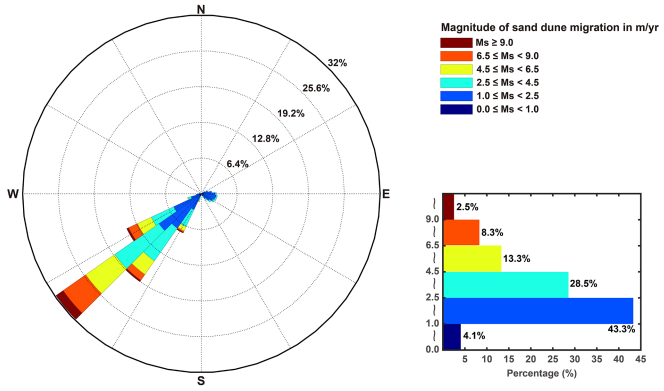

Fig. 15. Frequency distribution of the horizontal displacement velocity (m/year). Notably, the petals of the sand rose indicate the heading direction of the dune movements.

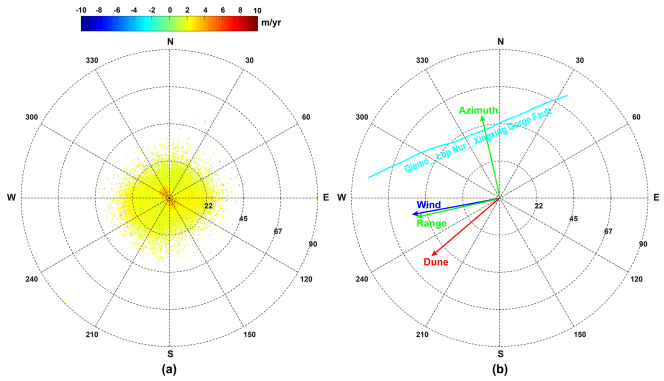

Fig. 16. (a) Distribution of the horizontal displacement velocity (m/year) considering different slope aspects (0°–360°) and different slope gradients (0°–90°) that were derived from the TerraSAR-X DEM. (b) Geometry relationship of the predominant wind direction (blue arrow), the predominant dune migration direction (red arrow), the Qiemo_Lop Nur_Xingxing Gorge Fault (cyan line), and the azimuth/range directions of SAR sensor (green arrows).

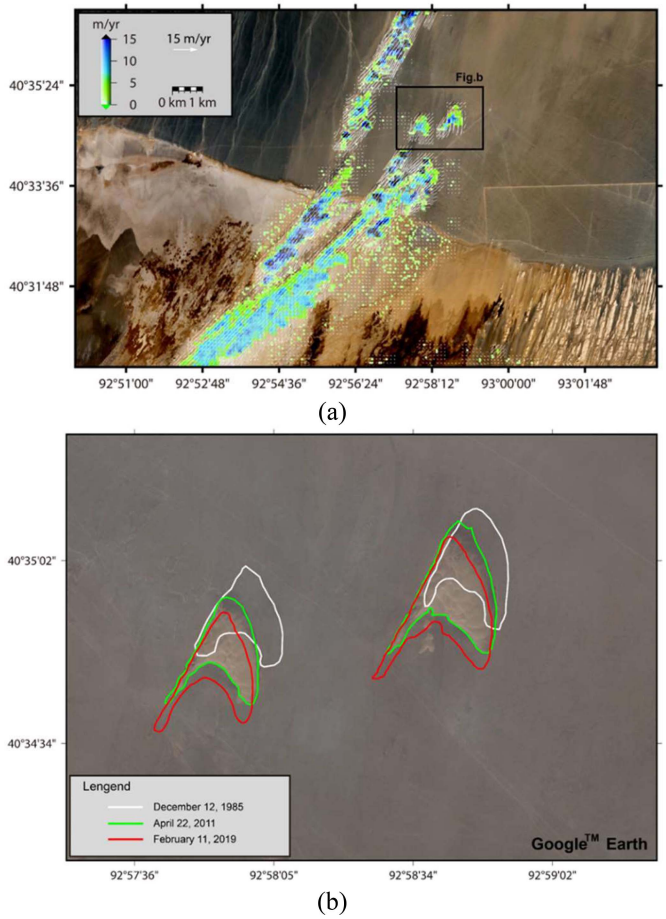

Fig. 17. (a) Enlarged view on the S2-derived displacement velocity (m/year) of the crescent dunes in the upward source region of Kumtag Desert. The background is the S2 composite image of red, green, and blue bands shot on September 7, 2016. (b) Temporal migration of the geographical location of the crescent dunes in the source region of Kumtag Desert indicated by the historical Google™ Earth images.

construct the causations of the strong scattering signals in SAR image, which then facilitates the performance of SAR offset-tracking technique in quantifying the movements of the feather-shaped dunes. Also, the predominant movement direction of the feather-shaped dunes presents as approximately parallel to the western Qiemo-Lop Nur-Xingxing Gorge Fault as displayed in Fig. 16(b). The formation of peculiar feather-shaped dunes was assumed as possibly triggered by the specific topography and its impacts on the local wind conditions. Comparatively, from the perspective of vertical dune displacement as shown in Fig. 11, the vertical displacement velocity showed smaller magnitudes with respect to that of EW and NS components, meaning the dune migration mainly occurred along the horizontal direction. Also, the dominant positive values in vertical component denote an accumulative tendency of sand–dust mass inside the Kumtag Desert.

As displayed in Fig. 16(a), the feather-shaped dunes moved mainly on the slope gradient with small values of around 0°–6°, and along the slope aspect of around 300°–350° toward the northwestern and around 120°–180° toward the southeastern. In other words, the sand transport over the feather-shaped dunes primarily occurred along both flanks of the pinna rachis. The spatial heterogeneity of the dune displacement velocity with respect to the local topography demonstrated by Fig. 16(a) can identify the characteristics of the microclimate inside the feather-shaped dunes. The specific spatial characteristics can be illuminated as the parallel strike of the pinna rachis of feather-shaped dunes compared to the radar flighting direction and dunes' vertical orientation toward the radar pulse signals. Besides, the displacement velocity in the ridges of feather-shaped dunes present larger magnitude than that of other portions. As displayed in Fig. 17 , according to the high-resolution Google™ Earth images and the spatial variations in dune migration patterns, the sand source region was identified. Specifically, flowing from the upward wind direction to the downward as shown in Figs. 17 and 18, the dune morphology develops gradually from the single crescent dunes, to the compound crescent dunes, then to the linear/longitudinal dunes, and finally to the feather-shaped dunes as the dominant dune pattern in Kumtag Desert. The maximal velocity of sand transport was observed mostly on the top ridge lines, or in a more vivid statement, the pinna rachises of the feather-shaped dunes.

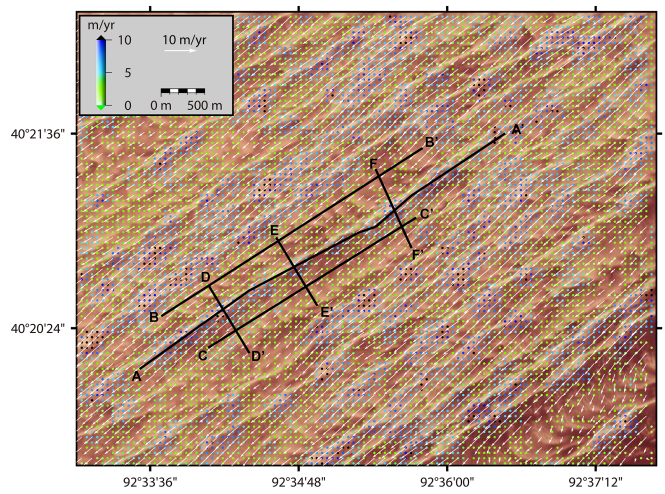

Fig. 18. Enlarged view on the S2-derived displacement velocity (m/year) of the feather-shaped dunes inside the Kumtag Desert. The background is the S2 composite image of red, green, and blue bands shot on September 7, 2016.

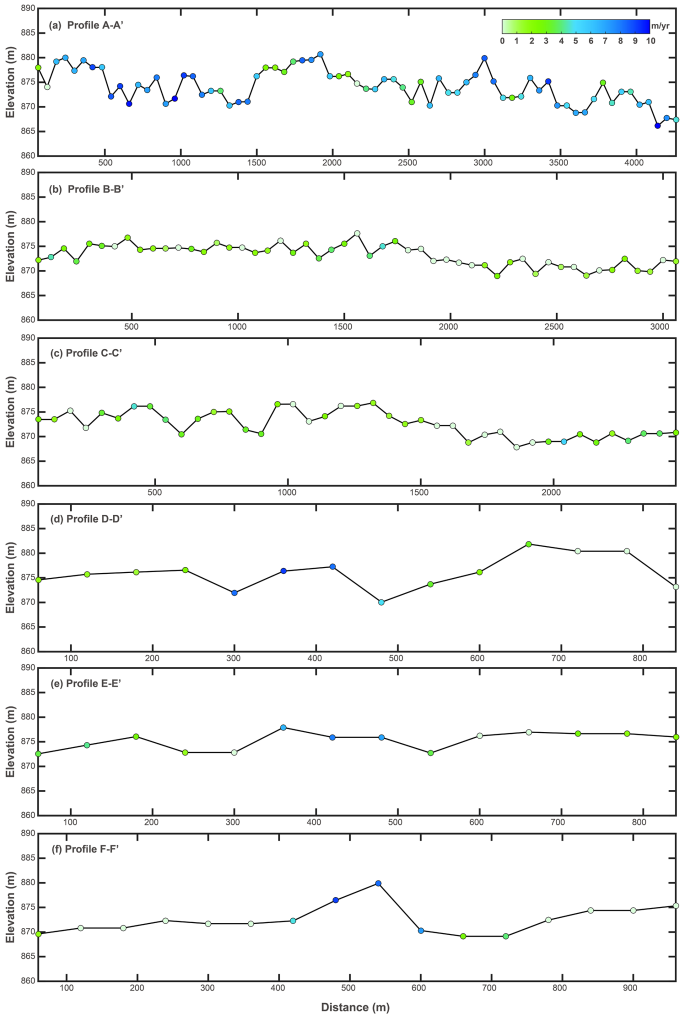

Fig. 19. Cross-comparison between the S2-derived average dune displacement velocity (m/year) and the local desert terrain along: (a) profile A-A′, (b) profile B-B′, (c) profile C-C′, (d) profile D-D′, (e) profile E-E′, and (f) profile F-F′.

To better illuminate the spatial dynamic characteristics of the feather-shaped dunes and their relationships with respect to the local topography, totally six profiles of A-A′ along the pinna rachis of the feather-shaped dunes constructed by the longitudinal barchan bridges, B-B′ along the upward gallery through the rami of the feather-shaped dunes constructed by the cambered transverse dunes, C-C′ along the downward gallery through the rami of the feather-shaped dunes constructed by the cambered transverse dunes, D-D′, E-E′, and F-F′ perpendicular to the pinna rachis were selected in Fig. 18. Subsequently, the displacement velocities against the ground surface elevation along these profiles were compared in Fig. 19. Specifically, the large displacement velocities are mainly concentrated in the pinna rachis of the feather-shaped dunes with the average of around 6.12 m/year on an average elevation of around 874.14 m. Comparatively, the one in the rami of the feather-shaped dunes has the average of around 2.46 m/year on an average elevation of around 872.91 m. Furthermore, the sand flux [41] in the pinna rachis was reckoned as around 4.45 m^2/year, larger than that in the rami. Besides, the displacement velocities along the pinna rachis were also changed intermittently with the alternate emergence of large values and small values, indicating the changeable microtopography along the pinna rachis.

VI. Conclusion

In this article, with the optical dataset of S2 and the SAR dataset of S1 as the test data, four different techniques of optical image cross-correlation, SAR offset-tracking, SBAS-InSAR, and InSAR coherence were combined to identify and quantify the time-series movements of peculiar feather-shaped dunes inside the Kumtag Desert. Although rarely used in existing studies on mobile desert, SAR offset-tracking was verified as useful for measuring the movements of these feather-shaped dunes in slant-range and azimuth directions. Except for identifying the active dune region as the conventional InSAR coherence has done, the methodology of combining optical and SAR observations in this article also possess the capability of measuring the migration magnitude and direction of the feather-shaped dunes from a multidimensional perspective of EW, NS, slant-range, and azimuth. Besides, 3-D displacement velocities of the feather-shaped dunes were innovatively inverted from the optical-derived EW/NS and the SAR-derived slant-range/LOS displacement results.

Furthermore, the temporal evolution of these dynamic characteristics exhibited a high-correlation with the local wind conditions. The optical-/SAR-derived displacement time series and velocity demonstrated that the possible migration activity mainly occurred in the windy summer and spring months, rather than the winter and autumn months. Notably, the temporal patterns were highly correlated with the local wind condition and its variations. Then, by deeply interpreting the spatial evolution, the sand transport was found mainly happened on the two flanks of the pinna rachis of the feather-shaped dunes with a relatively small slope gradient and a northwestern–southeastern facing slope aspect. This article sheds a bright light to investigate the

dynamic characteristics and their spatiotemporal evolution of the peculiar feather-shaped dunes inside the Kumtag Desert, with the complement of optical image cross-correlation, SAR offset-tracking, SBAS-InSAR, and InSAR coherence time series. In future article, deep interpretation on the multidimensional dune displacement characteristics can be helpful for further indicating the variations in near-ground atmospheric conditions of this vast desert without enough field measurements.

ACKNOWLEDGMENT

The COSI-Corr software developed by the California institute of technology was used to derive the optical image cross-correlation results. Also, the GAMMA software was the platform of processing the SAR datasets. Some figures in this article were plotted with the GMT software.

REFERENCES

[1] X. Wang, F. Chen, E. Hasi, and J. Li, "Desertification in China: An assessment," *Earth-Sci. Rev.*, vol. 88, pp. 188–206, 2008.
[2] G. Wu et al., "Physical geography," College teaching materials, 2000.
[3] L. Bruno, M. Horvat, and L. Raffaele, "Windblown sand along railway infrastructures: A review of challenges and mitigation measures," *J. Wind Eng. Ind. Aerodyn.*, vol. 177, pp. 340–365, 2018.
[4] A. Aili and N. T. Kim Oanh, "Effects of dust storm on public health in desert fringe area: Case study of northeast edge of Taklimakan Desert, China," *Atmos. Pollut. Res.*, vol. 6, pp. 805–814, 2015.
[5] R. A. Bagnold, *The Physics of Blown Sand and Desert Dunes*. London, U.K.: Methuen, 1941.
[6] Y. Wang, A. F. Stein, R. R. Draxler, J. D. de la Rosa, and X. Zhang, "Global sand and dust storms in 2008: Observation and HYSPLIT model verification," *Atmos. Environ.*, vol. 45, pp. 6368–6381, 2011.
[7] G. Sauermann, J. S. Andrade, L. P. Maia, U. M. S. Costa, A. D. Araujo, and H. J. Herrmann, "Wind velocity and sand transport on a barchan dune," *Geomorphology*, vol. 54, pp. 245–255, 2003.
[8] P. Vermeesch and S. Leprince, "A 45-year time series of dune mobility indicating constant windiness over the central Sahara," *Geophys. Res. Lett.*, vol. 39, no. 14, pp. L14401(1-5), 2012.
[9] N. Lancaster, "Winds and sand movements in the Namib sand sea," *Earth Surf. Process. Landforms*, vol. 10, pp. 607–619, 1985.
[10] C. M. Weaver and G. F. S. Wiggs, "Field measurements of mean and turbulent airflow over a barchan sand dune," *Geomorphology*, vol. 128, pp. 32–41, 2011.
[11] F. Ayoub et al., "Threshold for sand mobility on Mars calibrated from seasonal variations of sand flux," *Nature Commun.*, vol. 5, 2014, Art. no. 5096.
[12] X. Ren, X. Yang, Z. Wang, B. Zhu, D. Zhang, and P. Rioual, "Geochemical evidence of the sources of aeolian sands and their transport pathways in the Minqin Oasis, northwestern China," *Quaternary Int.*, vol. 334, no. 335, pp. 165–178, 2014.
[13] J. P. Avouac and S. Leprince, "Geodetic imaging using optical systems," *Treatise Geophys.*, vol. 3, pp. 387–424, 2015.
[14] C. H. Hugenholtz, N. Levin, T. E. Barchyn, and M. C. Baddock, "Remote sensing and spatial analysis of aeolian sand dunes: A review and outlook," *Earth-Sci. Rev.*, vol. 111, pp. 319–334, 2012.
[15] P. Vermeesch and N. Drake, "Remotely sensed dune celerity and sand flux measurements of the world's fastest barchans (Bodélé, Chad)," *Geophys. Res. Lett.*, vol. 35, no. 24, pp. L24404(1-6), 2008.
[16] M. Necsoiu, S. Leprince, D. M. Hooper, C. L. Dinwiddie, R. N. Mcginnis, and G. R. Walter, "Monitoring migration rates of an active subarctic dune field using optical imagery," *Remote Sens. Environ.*, vol. 113, pp. 2441–2447, 2009.
[17] E. Hermas, S. Leprince, and I. A. Elmagd, "Retrieving sand dune movements using sub-pixel correlation of multi-temporal optical remote sensing imagery, Northwest Sinai Peninsula, Egypt," *Remote Sens. Environ.*, vol. 121, pp. 51–60, 2012.
[18] S. P. Scheidt and N. Lancaster, "The application of COSI-Corr to determine dune system dynamics in the Southern Namib Desert using aster data," *Earth Surf. Process. Landforms.*, vol. 38, pp. 1004–1019, 2013.
[19] N. T. Bridges et al., "Earth-like sand fluxes on Mars," *Nature*, vol. 485, no. 7398, pp. 339–342, 2012.
[20] C. Ding et al., "Quantifying the spatio-temporal patterns of dune migration near Minqin Oasis in northwestern China with time series of Landsat-8 and Sentinel-2 observations," *Remote Sens. Environ.*, vol. 236, 2020, Art. no. 111498.
[21] E. Ali, W. Xu, and X. Ding, "Improved optical image matching time series inversion approach for monitoring dune migration in North Sinai Sand Sea: Algorithm procedure, application, and validation," *ISPRS J. Photogrammetry Remote Sens.*, vol. 164, pp. 106–124, 2020.
[22] C. Ding, G. Feng, M. Liao, and L. Zhang, "Change detection, risk assessment and mass balance of mobile dune fields near Dunhuang Oasis with optical imagery and global terrain datasets," *Int. J. Digit. Earth*, vol. 13, pp. 1604–1623, 2020.
[23] M. Liao et al., *Method and Practice of Radar Remote Sensing Monitoring of Landslide Deformation*. Beijing, China: Science Press, 2017.
[24] M. Abdelkareem, A. Gaber, F. Abdalla, and G. K. El-Din, "Use of optical and radar remote sensing satellites for identifying and monitoring active/inactive landforms in the driest desert in Saudi Arabia," *Geomorphology*, vol. 362, 2020, Art. no. 107197.
[25] D. G. Blumberg, "Analysis of large aeolian (wind-blown) bedforms using the Shuttle Radar Topography Mission (SRTM) digital elevation data," *Remote Sens. Environ.*, vol. 100, no. 2, pp. 179–189, 2006.
[26] X. T. Chang, J. Y. Guo, Y. H. Zhang, and X. Q. Wang, "On the application of DInSAR to deformation monitoring in desert areas," *Appl. Geophys.*, vol. 8, no. 1, pp. 86–93, 2011.
[27] X. T. Chang, J. Y. Guo, and X. Q. Wang, "Detecting the amount of eroded and deposited sand using DInSAR," *Terr. Atmos. Ocean. Sci.*, vol. 22, no. 2, pp. 187–194, 2011.
[28] M. Maghsoudi, A. Hajizadeh, M. A. Nezammahalleh, H. Seyedrezai, A. Jalali, and M. Mahzoun, "Interferometric synthetic aperture radar (INSAR) technology and geomorphology interpretation," *ISPRS Int. Arch. Photogrammetry Remote Sens. Spatial Inf. Sci.*, vol. 377, no. 107586, pp. 253–256, 2013.
[29] S. Havivi et al., "Mapping dune dynamics by InSAR coherence," *Earth Surf. Process. Landforms.*, vol. 43, no. 6, pp. 1229–1240, 2018.
[30] J.-R. Kim, C.-W. Lin, and S.-Y. Lin, "The use of InSAR phase coherence analyses for the monitoring of aeolian erosion," *Remote Sens.*, vol. 13, no. 12, 2021, Art. no. 2240.
[31] Y. Song et al., "Mapping the temporal and spatial changes in crescent dunes using an interferometric synthetic aperture radar temporal decorrelation model," *Aeolian Res.*, vol. 46, 2020, Art. no. 100616.
[32] J. M. Delgado Blasco, M. Chini, G. Verstraeten, and R. F. Hanssen, "Sand dune dynamics exploiting a fully automatic method using satellite SAR data," *Remote Sens.*, vol. 12, no. 23, 2020, Art. no. 3993.
[33] D. G. Blumberg, "Remote sensing of desert dune forms by polarimetric synthetic aperture radar (SAR)," *Remote Sens. Environ.*, vol. 65, no. 2, pp. 204–216, 1998.
[34] Z. Dong, J. Qu, G. Qian, and Z. Zhang, "Aeolian geomorphological regionalization of the Kumtag desert," *J. Desert Res.*, vol. 31, no. 4, pp. 805–814, 2011.
[35] K. Liao et al., "Intensity of sand-blown activities over feather-shaped sand ridge of Kumtag Desert," *J. Desert Res.*, vol. 28, no. 3, pp. 399–404, 2008.
[36] Z. Dong, J. Qu, Q. Lu, and G. Qian, "A discussion on feathery aeolian geomorphology in the Kumtagh Desert," *J. Desert Res.*, vol. 28, pp. 1005–1010, 2008.
[37] Z. Zhu, Z. Wu, S. Liu, and X. Di, *The General Introduction to Chinese Deserts*. Beijing, China: Science Press, 1980.
[38] J. Qu et al., "Study on formation mechanism of feather-shaped sand ridge in Kumtag Desert," *J. Desert Res.*, vol. 27, no. 3, pp. 349–353, 2007.
[39] J. Wang et al., "Preliminary results of scientific expedition to Kumtag Desert," *Gansu Sci. Technol.*, vol. 21, no. 10, pp. 6–8, 2005.
[40] Y. Lan, "The study of the historical region prototype of the north-south silk road in journey to the west-on the regional generalization and text narration in the ancient Chinese landscape attachment," *J. Tsinghua Univ.*, vol. 34, no. 05, pp. 28–41, 2019.
[41] S. Fryberger and G. Dean, "Dune forms and wind regime," Professional Paper 1052, in *A Study of Global Sand Seas*, E. McKee, Ed. Reston, VA, USA: United States Geological Survey, 1979, pp. 137–169.
[42] S. Leprince, S. Barbot, F. Ayoub, and J.-P. Avouac, "Automatic and precise orthorectication, coregistration, and subpixel correlation of satellite images, application to ground deformation measurements," *IEEE Trans. Geosci. Remote Sens.*, vol. 45, no. 6, pp. 1529–1558, Jun. 2007.
[43] C. Ding, G. Feng, Z. Li, X. Shan, Y. Du, and H. Wang, "Spatio-temporal error sources analysis and accuracy improvement in Landsat 8 image ground displacement measurements," *Remote Sens.*, vol. 8, no. 11, 2016, Art. no. 937.

[44] F. Casu, A. Manconi, A. Pepe, and R. Lanari, "Deformation time-series generation in areas characterized by large displacement dynamics: The SAR amplitude pixel-offset SBAS technique," *IEEE Trans. Geosci. Remote Sens.*, vol. 49, no. 7, pp. 2752–2763, Jul. 2011, doi: 10.1109/TGRS.2010.2104325.

[45] P. Berardino, G. Fornaro, R. Lanari, and E. Sansosti, "A new algorithm for surface deformation monitoring based on small baseline differential SAR interferograms," *IEEE Trans. Geosci. Remote Sens.*, vol. 40, no. 11, pp. 2375–2383, Nov. 2002.

[46] R. Touzi, A. Lopes, J. Bruniquel, and P. W. Vachon, "Coherence estimation for SAR imagery," *IEEE Trans. Geosci. Remote Sens.*, vol. 37, no. 1, pp. 135–149, Jan. 1999.

Chao Ding received the B.Eng. degree in surveying and mapping engineering from the Shandong University of Technology, Zibo, China, in 2014, the M.A degree in surveying and mapping engineering from the Central South University, Changsha, China, in 2017, and the Ph.D. degree in photogrammetry and remote sensing from the State Key Laboratory of Information Engineering in Surveying, Mapping and Remote Sensing, Wuhan University, Wuhan, China, in 2020.

He is currently a Lecturer with the Shandong University of Technology, Zibo, China. His research interests include the displacement quantification of dune migration, landslide creeping, and earthquake with the image geodesy technique.

Guangcai Feng received the master's degree in surveying engineering from the Central South University, Changsha, China, in 2006, and the Ph.D. degree in geophysics and geodesy from The Hong Kong Polytechnic University, Hong Kong, in 2011.

He is currently a Full Professor with the Department of Surveying and Remote Sensing, School of Geoscience and Info-Physics, Central South University. His research interests include interferometric synthetic aperture radar for inverting source parameters of earthquakes and ground deformation monitoring in urban areas.

Lu Zhang received the B.Eng. and M.Eng. degrees in computer science and technology from the Wuhan University of Hydraulic and Electrical Engineering, Wuhan, China, in 1997 and 2000, respectively, and the Ph.D. degree in photogrammetry and remote sensing from the Wuhan University, Wuhan, China, in 2005.

From 2005 to 2007, he was a Postdoctoral Research Fellow with the Institute of Space and Earth Information Science, The Chinese University of Hong Kong, Hong Kong. Since 2007, he has been with the State Key Laboratory of Information Engineering in Surveying, Mapping and Remote Sensing, Wuhan University, where he became a Full Professor in 2013. He has been involved in several research projects funded by the National Natural Science Foundation of China and the Ministry of Science and Technology. He has authored about 30 peer-reviewed scientific papers. His research interests include synthetic aperture radar interferometry as well as remote sensing classification and change detection.

Mingsheng Liao received the B.S. degree in electronic engineering from the Wuhan Technical University of Surveying and Mapping (WTUSM), Wuhan, China, in 1982, the M.A. degree in electronic and information engineering from the Huazhong University of Science and Technology, Wuhan, China, in 1985, and the Ph.D. degree in photogrammetry and remote sensing from the WTUSM, in 2000.

He has been with the State Key Laboratory of Information Engineering in Surveying, Mapping and Remote Sensing, Wuhan University, Wuhan, China, where he became a Professor in 1997. He is the Principal Investigator (PI) of several projects funded by the Ministry of Science and Technology (MOST) China and the Natural Science Foundation of China. He is also the Co-PI of the ESA-MOST Cooperative Dragon I during 2004–2008, II during 2008–2012, III during 2012–2016, and IV during 2016–2020 projects. He has authored more than 60 peer-reviewed journal papers and several book chapters focused on synthetic aperture radar interferometry techniques and applications. His research interests include remote sensing image processing and analysis, algorithms for interferometric synthetic aperture radar, integration and fusion of multisource spatial information, and application of remote sensing data.